NANO LETTERS

Letter

pubs.acs.org/NanoLett

Controlling Nanowire Growth by Light

G. Di Martino,[*,†] F. B. Michaelis,[‡] A. R. Salmon,[†,§] S. Hofmann,[*,‡] and J. J. Baumberg[*,†]

[†]NanoPhotonics Centre, Cavendish Laboratory, University of Cambridge, Cambridge CB3 0HE, United Kingdom

[‡]Department of Engineering, University of Cambridge, Cambridge CB3 0FA, United Kingdom

[§]Department of Chemistry, University of Cambridge, Cambridge CB2 1EW, United Kingdom

Supporting Information

ABSTRACT: Individual Au catalyst nanoparticles are used for selective laser-induced chemical vapor deposition of single germanium nanowires. Dark-field scattering reveals in real time the optical signatures of all key constituent growth processes. Growth is initially triggered by plasmonic absorption in the Au catalyst, while once nucleated the growing Ge nanowire supports magnetic and electric resonances that then dominate the laser interactions. This spectroscopic understanding allows real-time laser feedback that is crucial toward realizing the full potential of controlling nanomaterial growth by light.

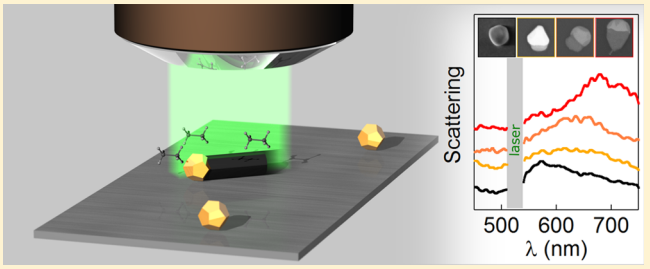

KEYWORDS: *Catalysis, laser-induced chemical vapor deposition, germanium nanowires, plasmonics, dark field spectroscopy, magnetic resonances*

Bottom-up or self-assembly approaches to nanofabrication such as the catalytic growth of semiconductor nanowires (NWs) offer unique compositional and structural control and versatility, opening pathways to new functionalities in a wide range of applications including electronics, thermo-electrics, energy storage and conversion, and biomedical sensors.[1−7] In the vapor−liquid−solid (VLS) and vapor−solid−solid (VSS) growth mechanisms, a liquid or solid catalyst such as a Au nanoparticle selectively dissociates a vapor phase precursor and mediates anisotropic NW crystal growth.[8,9] This has been extensively explored for groups IV,[10,11] III−V,[12,13] and II−VI[14,15] semiconductor materials and their device integration. Typically the reaction is triggered by globally heating the sample to temperatures in excess of 300 °C, which not only limits the choice of substrate and device integration pathways but also acts on all catalyst particles with the same precursor and conditions, limiting the versatility of the process. As a result, a range of local heating strategies have been explored in various processes including laser irradiation.[16,17] In this way, not only the catalytic but also the plasmonic properties of Au nanoparticles can be exploited, opening pathways for selective and effective local excitation at the subdiffraction level. The potential of such approaches, often termed plasmon-assisted chemical vapor deposition (CVD), has been highlighted already by a number of reports,[18,19] where the chemical growth reactions could be triggered selectively with high spatial resolution. However, understanding of the complex light-matter interactions during such laser-induced growth remains rudimentary and detailed structural growth control and the full potential of this approach could not be realized so far.

Here we study laser-driven catalytic nanowire CVD and show that the growth process can not only be optically powered but also monitored in real-time by optical spectroscopy at the individual nanoparticle level, which in combination allows a feedback process that is crucial to growth control. We find that the selectivity of the process is only initially given by the plasmonic absorption in the supported Au catalyst nanoparticle, while once nucleated the growing Ge nanowire supports magnetic and electric resonant modes that then dominate the laser interactions. This results in a process-dependent increase in absorption cross-section, and to achieve NW growth selectivity we show that the laser power has to be reduced accordingly. When carefully controlled the growth process can be maintained at very low laser powers, and is extremely efficient. This spectroscopic technique also enables us to follow the evolution of NW morphology during growth. We focus on Au catalyzed Ge NW CVD for which the thermal growth mechanisms have been well studied[20] and use it as model system to reveal the in situ optical signatures that enable tracking of the key processes of laser-driven CVD. Key characteristics, such as diameter and change in length of the NWs, can be identified from the optical signatures in the scattering signal. Moreover VLS and VSS growth mechanisms become distinguishable by analyzing such optical spectra. The spectroscopic feedback and insights gained are a key step toward realizing the full potential of controlling nanomaterial growth by light.

We use laser irradiation and selective absorption to locally heat and trigger reactions on individual supported catalyst nanoparticles in a gaseous precursor atmosphere (Figure 1a,b).

Received: July 27, 2015
Revised: October 20, 2015
Published: October 26, 2015

DOI: 10.1021/acs.nanolett.5b02953
Nano Lett. 2015, 15, 7452−7457

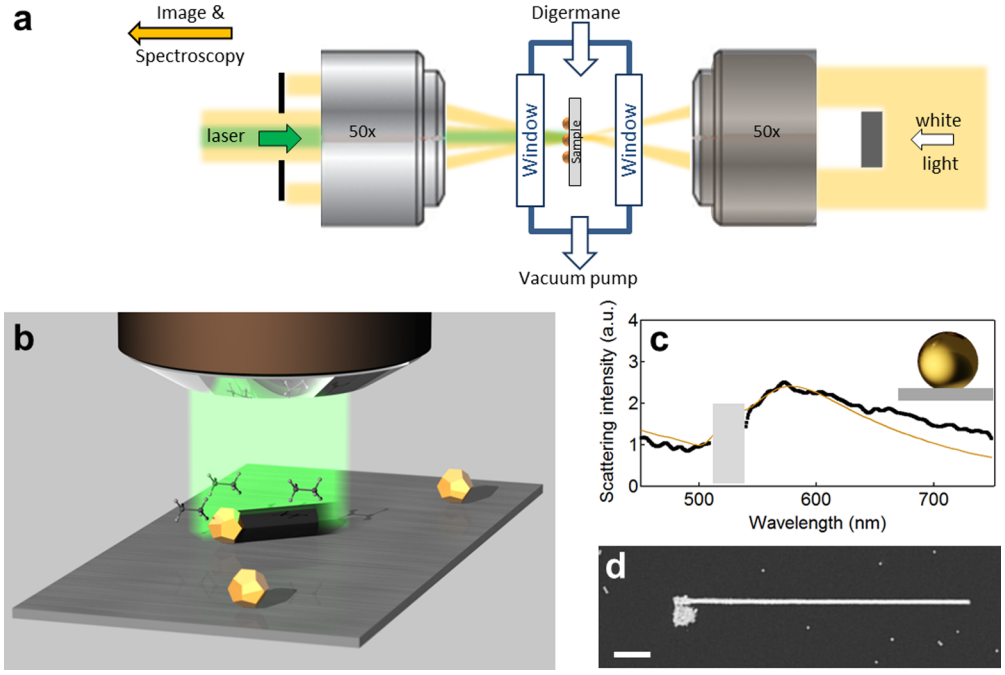

Figure 1. Experimental laser-induced CVD setup. (a) Configuration for optical growth monitored by dark-field scattering, sample mounted in a vacuum chamber and back illuminated by high-angle white light with only low-angle scattered light collected, pump 532 nm laser focused to 1 μm spot size. (b) Sketch of PLiCVD triggering Ge NW growth on the illuminated Au NP. (c) Typical initial scattering spectrum (black) of Au NP (points around laser line removed) with simulated spectrum (yellow) of 140 nm faceted Au sphere on a 20 nm thick silicon nitride substrate. (d) Long Ge nanowire grown, scale bar 2 μm.

We use diluted Ge_2H_6 as the precursor (0.2% in Ar, ~10 mbar total pressure during growth) and a customized stainless-steel vacuum chamber (base pressure ~10^{-7} mbar) in which we selectively illuminate well-separated (average distance >5 μm) 140 nm diameter Au nanoparticles (NPs) on a 20 nm thick transparent silicon nitride membrane with a continuous wave laser at λ = 532 nm. This wavelength is close to the plasmonic resonance of each Au NP, centered around 580 nm. The Au NPs are characterized by strong enhanced light absorption in this spectral region and are thus rapidly and locally heated by the laser. This leads to catalytic precursor dissociation and upon Ge supersaturation of the Au NP leads to Ge NW nucleation and growth. The reaction sequence and Ge growth lead in turn to an ever changing, process-dependent, optical absorption profile, which rapidly becomes no longer dominated by the Au plasmon and to which the laser power has to be adapted, as we discuss below. Because the laser spot size is ~1 μm and the collection region for spectroscopy is ~2 μm, only one NP is illuminated and characterized at any time. Using different off-resonant laser wavelengths (e.g., 780 nm) the initial power input required to trigger the catalytic Ge growth is much higher (>10×). This highlights the selective and effective local excitation of the process. Figure 1d highlights has Ge NW growth is catalyzed only at the particle under the focal spot, leaving nearby NPs unreacted and the substrate uncoated by Ge. Smaller NPs have also been tested (~80 nm), where the plasmon resonance remains spectrally close to the 532 nm laser. Although the technique is indeed applicable to smaller NPs and hence smaller NW diameters, the reduced scattering intensities with these smaller sizes makes resolving growth details increasingly difficult. As a result for our studies here in the current optical setup and to focus on understanding, we mainly used 140 nm diameter Au NPs. We investigated extensive libraries with different growth parameters by translating different Au NPs under the laser focus, allowing rapid, facile combinatorial mapping and screening of the CVD parameter space, which is arduous with conventional global back heating. We can check the Au NPs via their initial scattering spectra, automatically excluding dimers, agglomerates, or oversized NPs that do not show the characteristic resonance expected for a 140 nm Au NP (Figure 1c). Dark-field spectra are collected by scattering unpolarized white light focused from the back of the transparent membrane supporting the Au NPs and using notch filters to remove the laser line. This ensures the same initial conditions in all cases and provides good reproducibility.

Upon laser illuminating each Au NP, it heats up and starts reacting with the Ge_2H_6 precursor. Figure 2 shows a postgrowth scanning electron microscopy (SEM) image series representative of the initial Ge NW growth stages (Figure 2a–d, see Methods), together with the corresponding optical dark-field scattering spectra recorded in situ (Figure 2e). The atomic number (Z) contrast of the backscatter electron detector allows clear differentiation between the growing Ge crystal and the Au-based catalyst in the SEM images, which we also confirm by energy-dispersive X-ray spectroscopy (EDX, see Supporting Information Figure S1). To verify our assignments, we also record postgrowth optical scattering spectra, which do not show any significant changes from the spectra we record during the final stage of our growth process (see Supporting Information Figure S2), corroborating our interpretation below. As soon as germanium nucleates from the Au NP, there is a redshift and clear change in the scattering spectrum (Figure 2e). As the Ge crystal grows, the composite nanostructure starts to absorb more and more light as the optical cross-section increases, which can also be observed from the rise in scattering strength. If the laser power is not reduced accordingly to keep the temperature constant, this leads to detrimental overheating. The temperatures are then high

DOI: 10.1021/acs.nanolett.5b02953
Nano Lett. 2015, 15, 7452–7457

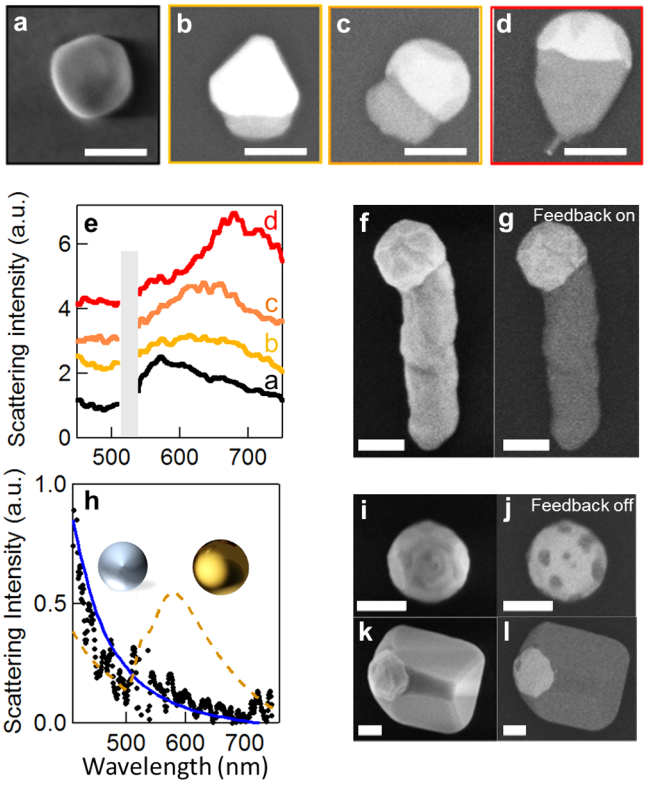

Figure 2. Evolution of NW growth. (a) SEM secondary electron (SE) image of Au NP before growth. (b–d) High-angle backscattered electron (HA-BSE) SEM images of Ge NWs in early stage growth. (e) Dark-field scattering spectra of (a–d), curves offset for clarity. (f,g) SE and HA-BSE images of Ge NW grown implementing feedback, giving controlled NW growth. (h) In-situ scattering spectrum (black) of overheated system shown in (i) SE and panel (j) HA-BSE images with simulated scattering spectrum of 130 nm SiO_2 sphere (blue) and 140 nm faceted Au sphere (yellow). (k) SE and (l) HA-BSE images of a Au NP together with Ge agglomerate grown by pyrolytic deposition due to overheating. No feedback control is implemented in (i–l). Scale bars are all 100 nm.

enough to lose the selectivity of the catalytic NW growth process and instead results in nonselective pyrolytic Ge overgrowth, creating an agglomerate of Ge material and faceted Ge crystalline particles (Figure 2k–l). The first symptom of such overheating is promptly detected by our in situ dark-field spectroscopy, appearing as strong blue scattering (Figure 2h), which fits well to modeled scattering from a dielectric alloyed sphere (blue line). A plausible explanation for this suggests the degeneration of the nanostructure into an agglomerate of interspersed Ge and Au clusters, arranged in a disordered matrix. This yields an overall dielectric-like (nonmetallic) optical response to the structure. Interestingly, we find in this case different early stage Au–Ge morphologies (Figure 2i,j) from the degeneration of the growth process. In order to avoid this overheating, we thus use the scattering intensity as a control signal to directly adjust the power of the laser (see Supporting Information Figure S3). By implementing this feedback, we can maintain the catalytic process to be dominant and grow Ge NWs (Figure 2f,g). It is therefore clear that real time monitoring of the scattering signal and adapting the laser power to the changing absorption behavior of the growing nanostructure is of paramount importance.

With the parameters used here, we generally observe two types of Ge NW growth dynamics, each characterized by a different evolution of the scattering spectra as highlighted by Figure 3. In type A (Figure 3a–f), a continuous redshift of the scattering peak is seen, reaching a wavelength of 800 nm by the end of the growth process (Figure 3e). The resulting Ge NW always shows an irregular, wormlike shape (Figure 3a–c) with diameters on the order of 130 nm. The Au NP is at the tip of the Ge NW (Figure 3d) with the catalyst-NW interface at postgrowth stage being often very nonplanar and irregular (Figure 3c,d). Moreover, the growth rate we extrapolate for this case is quite slow, ~0.04 nm/sec (see Supporting Information Figure S4). For type B, we observe a more complex evolution of the scattering spectra with an initial redshift suddenly switching to a double peak (Figure 3k). The resulting NWs in this case are comparatively much straighter (Figure 3g,i), and their average diameter is always larger (of order 180 nm). The catalyst–NW interface now also appears more planar (Figure

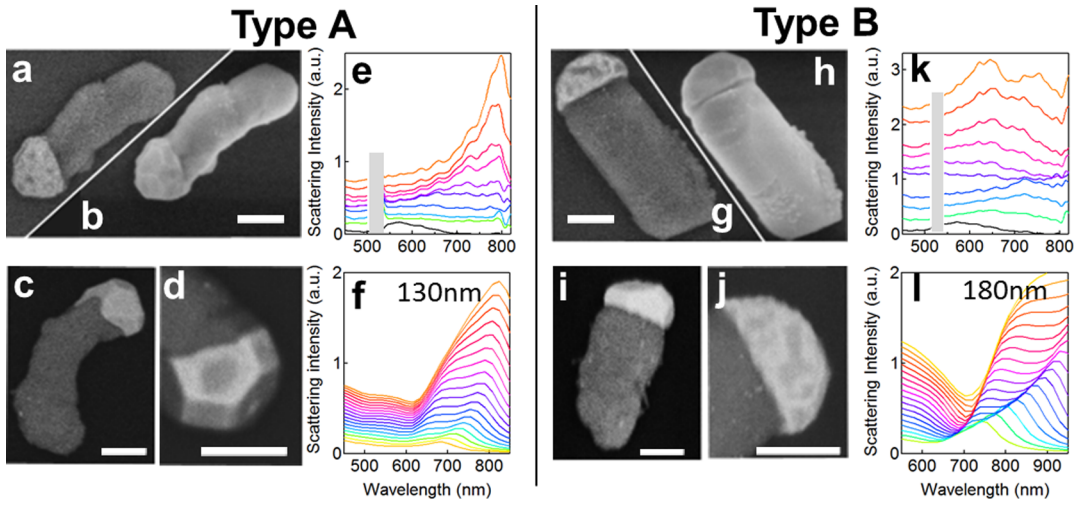

Figure 3. Dynamics of Type A,B growth. (a,c,d,g,i,j) High-angle backscattered SEM images (giving compositional contrast) and (b,h) secondary electron SEM images (topology contrast). Scale bars are 100 nm. (e,k) In situ dark-field scattering spectra of NW shown in (a,b), and (g,h), respectively. Offsets added for clarity. (f,l) Finite-difference time-domain simulating scattering spectra for Ge cylinder with increasing length of 130 and 180 nm diameters, respectively.

DOI: 10.1021/acs.nanolett.5b02953
Nano Lett. 2015, 15, 7452–7457

3g–j). Moreover for type B the growth rate is nearly a hundred-fold faster, ~2.7 nm/sec (see Supporting Information Figure S4). Type B growth dynamics occur for slower laser feedback, when the laser power is reduced less rapidly (see Methods). Hence higher local growth temperatures occur for type B compared to type A and, as discussed below, the observed differences can be rationalized by assuming two different growth mechanisms, a VSS-type mechanism with a solid catalyst particle for type A and a VLS growth mechanism for type B, where the catalyst forms a liquid alloy.[20,21]

We previously carried out a range of detailed studies on thermal catalytic NW CVD, highlighting how kinetically driven supersaturations determine the catalyst phase, and the important consequences for NW growth from solid versus liquid catalyst particles.[20,21] For the first time, we connect here such levels of growth detail to the laser-driven process. It is well-known that the simple Au–Ge eutectic phase diagram for the bulk equilibrium (eutectic temperature T_e = 361 °C at 28 atom % Ge[22]) does not fully capture the phase behavior for catalytic growth on the nanoscale. Hence catalyst liquefaction can be observed well below T_e.[21] Nonetheless, the higher the laser power, the higher the expected local temperature and the more likely catalyst liquefaction will occur. This can therefore account for all of the differences observed between type A and B nanowires. To first order, the NW diameter clearly relates to the catalyst particle diameter, but as shown previously in detail for thermal CVD with catalyst liquefaction (VLS mechanism) the Ge solubility is much higher hence increasing the catalyst (alloy) particle volume.[11] At the same time, the wetting angle of the catalyst alloy at the tip of the growing NW is modified compared to a crystalline catalyst. This results here in larger NW diameters for the VLS case. For the VSS mechanism, the gas exposures here appear too high given the reduced diffusivities, which hence leads to defective, irregular NW growth.

Understanding the experimentally observed scattering spectra (Figure 3e,k) requires further interpretation. We therefore model our system using the full geometry and material parameters of Ge and Au. In Figure 3, we show simulated scattering spectra of Ge nanocylinders of increasing length with different diameters placed on silicon nitride membranes. Scattering from the modeled 130 and 180 nm wide Ge nanocylinders (Figure 3f,l) is able to reproduce the red-shifting resonance coming from the elongation of Ge NWs (Figure 3e,k respectively) and the multiple peaks observed in the type B NWs (Figure 3k), showing in general good agreement with the experimental data. Indeed our simulations show that distinct multiple peaks start to be visible for diameters larger than 140 nm, allowing as a result the differentiation of the spectral signatures of 130 and 180 nm wide Ge nanocylinders. The role of Ge in the scattering spectra is of primary importance in providing key information about the growth process and hence is discussed further in the following section. This indicates that we are able to directly discern both the type of growth process, as well as the NW diameter directly from spectroscopy.

In contrast to metallic nanoparticles, for which the resonant scattering is dominated by electric resonances, dielectric nanoparticles can display both electric and magnetic dipole resonances simultaneously excited inside the particle. High-index dielectric or semiconductor nanostructures support (Mie-like) geometrical resonances in the visible spectral range,[23,24] driven by displacement currents.[25] NWs support a limited number of transverse-electric (TE) and transverse-magnetic (TM) resonances, which increase in number as their diameter is increased,[26] and which can be spectrally tuned by varying the NW length and diameter.[27] Sufficiently small diameter NWs (<30 nm) are predicted to support only the fundamental transverse-magnetic mode[26] while NWs possess a very strong polarization dependence, decreasing with increasing diameter.[26] However, as the in situ scattering measured here is rather weak and from unpolarised light, higher brightness sources are required to exploit this information (see Supporting Information Figure S5). Because the scattering spectrum of high refractive index nanowires depends strongly on diameter, the presence of two distinct diameters from each type of growth observed here thus accounts for the distinct scattering spectra found (Figure 3e,k).

We use numerical simulations to systematically study the resonant properties of Ge nanocylinders and thus understand the spectral dynamics observed during Ge NW growth. For simplicity, we show here results for Ge nanocylinders with incident light polarized along their length and incident normally (Figure 4b) but similar results are found for orthogonal

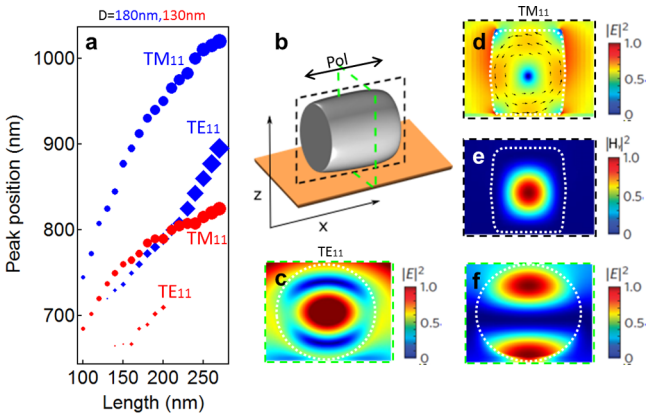

Figure 4. Simulated resonant field modes for Ge nanocylinder. (a) Peak positions of different resonant modes, transverse magnetic (TM, ●) and transverse electric (TE, ■), for increasing length of Ge nanocylinder, of diameters 130 nm (red) and 180 nm (blue). Marker size indicates intensity of scattering. (b) Simulated geometry. (c–f) Near-field distributions for Ge nanocylinder with diameter 130 nm and length 270 nm: (c) $E(yz)$ at resonant wavelength of 650 nm, (d) $E(xy)$ at resonant wavelength of 840 nm, (e) $H_y(xz)$ and (f) $E(yz)$ at resonant wavelength of 840 nm. In all simulations, incident Gaussian beam is polarized along x and propagating along $-z$.

polarizations (see Supporting Information Figure S5). The spectral positions of the resonances for different modes excited inside the NW show a general redshift with increasing length of the cylinder (Figure 4a). This enables us to follow the elongation of NWs during growth. By analyzing their near-field profile in the xy plane, the resonances can be assigned,[26] revealing optical fields associated with both the dominant TE_{11} (Figure 4c) and TM_{11} (Figure 4f) modes. This confirms the excitation of both electric and magnetic resonances in our NWs. In the long wavelength region, the circulation of the electric field in the xz plane (Figure 4d) produces a strong magnetic field component along y (Figure 4e), responsible for the strong magnetic scattering of the TM_{11} mode. Only in large diameter cylinders (Figure 4a) does scattering from the TE_{11} mode contribute significantly.

DOI: 10.1021/acs.nanolett.5b02953
Nano Lett. 2015, 15, 7452–7457

Our results show the capability to selectively grow single NWs by optically monitoring the catalytic NW growth and hence to be able to implement real-time feedback, adapting the laser power to the ever changing optical cross-section of the growing nanostructure.[28,29] At the initial stage of NW PLiCVD, we exploit the plasmonic absorption in an individual Au NP, which then selectively reacts with the Ge precursor following a VLS or VSS mechanism. Our results show that the nucleated and growing Ge crystal supports magnetic and electric resonant modes. The resulting scattering spectrum of the Ge NW strongly depends on its diameter as well as on its length with large resonant absorption enhancements at specific wavelengths.[26] Here we locally heat single NPs using laser irradiation to harness the catalytic and plasmonic properties of Au. This technique operates at very low laser powers making it ideally suited to combine with other in situ characterization techniques, such as electron microscopy,[30] to provide powerful future metrology, and correlative imaging platforms. Exploiting this enhanced absorption with the thin support membrane allows us to drive the catalytic growth reaction at low laser power (0.2−0.6 mW), more than an order of magnitude lower than previous literature results, where powers >20 mW were needed to trigger the reaction.[18]

Our assignments of the optical signatures also allow us to spectrally follow the NW evolution and in particular to distinguish two types of Ge NW growth dynamics. We propose that our laser feedback operates so as to either keep the Au NP solid or to locally increase the temperature enough to liquefy the catalyst. Such spectroscopic feedback coupled with optical irradiation forms a unique capability to direct nanomaterial growth down specific pathways. We focused here on Ge NW growth, but the approach of plasmonic-initiated catalytic growth is applicable to a wide range of material systems, such as Au catalyzed group V, group III−V, and group II−VI semiconductor NWs and their heterostructures, opening a wide range of applications.

Methods. *Sample Preparation.* The 138 ± 5 nm diameter Au NPs were made in three-seeded growth steps following the method of Ziegler et al.[31] The Au NPs were characterized by scanning transmission electron microscopy with the mean diameter and standard deviation given from 50 measurements. The Au NPs were deposited onto silicon nitride 20 nm thick TEM grids (SiMPore Inc.) by drop casting. In a typical deposition, the as-prepared Au NP suspension was diluted by a factor of 10 (final concentration $\sim 10^8$ ml^{-1}) and a portion was pipetted onto the grid. After 3 min, deionized water was added and then the suspension was wicked away using lint-free paper. By the same wicking method, the grid was twice rinsed with deionized water. The gas mixture used for these growth experiments is 0.2% digermane balanced in argon with a gas pressure during growth of 10 mbar (no gas flow).

Optical Setup. The sample is mounted in a custom-built low volume optical-accessible vacuum chamber and is back illuminated by high-angle white light incident through a 50×/0.50NA dark-field objective (Olympus BD LMPLFLN) in an optical dark field configuration with only low-angle scattered light collected by a 50×/0.50NA (Mitutoyo BF G Plan Apo) objective, specifically designed for compensating transmission through the 3.5 mm BK7 glass window of the vacuum chamber. The dark-field scattered light is then sent to a CCD camera (Infinity) and spectrometer (Ocean Optics QE65000) for spectral analysis. At the same time, a 532 nm CW laser is focused onto the sample through the Plan Apo objective with a final spot size of 1 μm. The power of the laser is modified by rotation of a computer-controlled half waveplate located just before a polarizer. Two notch filters screen the scattered laser light avoiding its detection on the CCD and spectrometer.

Power Intensity and Feedback Control. Initial laser powers of 0.6 mW are focused onto the 1 μm spot, which is the minimum power needed to trigger growth. The feedback control reduces the power of the laser when the scattering intensity, integrated over the 650−700 nm region, exceeds set thresholds. We set a first intensity threshold at twice the initial scattering intensity after which the laser power is reduced by 18% and 15% for type A and type B growth, respectively, whenever an increase of the scattering signal is detected. The integrated scattering intensity continues to rise until a second intensity threshold (at six times the initial scattering intensity) after which the laser power is now reduced by 28% and 25% for type A and type B growth, respectively. By this method, we realize two different growth recipes resulting in the two different growth dynamics we have identified, characterized by a faster (type A) or slower (type B) laser power reduction. In these recipes, different local growth temperatures can be achieved. The overall result is an initial fast decrease of the laser power until a stationary regime is reached with eventual constant intensities of 0.1−0.2 mW (see Supporting Information Figure S3).

Electron Microscopy. A Hitachi S-5500 field emission scanning electron microscope (SEM) was used to characterize Au NPs and the grown Ge NWs directly on the 20 nm thick Si_3N_4 membrane TEM grid.

Numerical Simulations. A commercial simulator based on the finite-difference time-domain method was used to perform the calculations of the far-field extinction spectra and near-field distributions (Lumerical Solutions Inc.). Perfectly matched layer (PML) absorbing boundaries conditions have been implemented. The simulated source is a broadband Gaussian beam polarized along x (or y, see Supporting Information Figure S5) and propagating along $-z$.

■ ASSOCIATED CONTENT

Supporting Information

The Supporting Information is available free of charge on the ACS Publications website at DOI: 10.1021/acs.nanolett.5b02953.

Material analysis of a Ge NW using energy-dispersive X-ray (EDX) spectroscopy, analysis proving quenching of the system, details on laser power reduction due to feedback control, growth rate of the two different growth mechanisms, and influence of polarization. Source date can be found at https://www.repository.cam.ac.uk/handle/1810/252442(PDF)

■ AUTHOR INFORMATION

Corresponding Authors

*E-mail: gd392@cam.ac.uk.
*E-mail: sh315@cam.ac.uk.
*E-mail: jjb12@cam.ac.uk.

Author Contributions

Experiments were performed by G.D. with support for the chemical nanoassembly from A.S. and growth calibrations of B.M. The software and the experimental setup were developed by G.D. and B.M. Modeling and simulations were performed by

DOI: 10.1021/acs.nanolett.5b02953
Nano Lett. 2015, 15, 7452−7457

G.D., S.H., and J.J.B. designed the experiments and coordinated the analysis. All authors contributed to the manuscript.

Notes

The authors declare no competing financial interest.

■ ACKNOWLEDGMENTS

We acknowledge financial support from EPSRC Grant EP/G060649/1, EP/L027151/1, EP/G037221/1, EPSRC NanoDTC, and ERC Grant LINASS 320503. S.H. acknowledges funding from ERC Grant InsituNANO 279342. We acknowledge valuable discussions with Angela Demetriadou and Federico Panciera during different stages of the research.

■ REFERENCES

(1) Ionescu, A. M.; Riel, H. *Nature* **2011**, *479* (7373), 329−337.
(2) Li, Y.; Qian, F.; Xiang, J.; Lieber, C. M. *Mater. Today* **2006**, *9* (10), 18−27.
(3) Hu, J.; Odom, T. W.; Lieber, C. M. *Acc. Chem. Res.* **1999**, *32* (5), 435−445.
(4) Fan, H. J.; Werner, P.; Zacharias, M. *Small* **2006**, *2* (6), 700−717.
(5) Chan, C. K.; Zhang, X. F.; Cui, Y. *Nano Lett.* **2008**, *8* (1), 307−309.
(6) Zheng, G.; Patolsky, F.; Cui, Y.; Wang, W. U.; Lieber, C. M. *Nat. Biotechnol.* **2005**, *23* (10), 1294−1301.
(7) Hochbaum, A. I.; Chen, R.; Delgado, R. D.; Liang, W.; Garnett, E. C.; Najarian, M.; Majumdar, A.; Yang, P. *Nature* **2008**, *451* (7175), 163−167.
(8) Wagner, R. S.; Ellis, W. C. *Appl. Phys. Lett.* **1964**, *4* (5), 89−90.
(9) Hofmann, S.; Sharma, R.; Wirth, C. T.; Cervantes-Sodi, F.; Ducati, C.; Kasama, T.; Dunin-Borkowski, R. E.; Drucker, J.; Bennett, P.; Robertson, J. *Nat. Mater.* **2008**, *7* (5), 372−375.
(10) Cui, Y.; Lieber, C. M. *Science* **2001**, *291* (5505), 851−853.
(11) Kodambaka, S.; Tersoff, J.; Reuter, M. C.; Ross, F. M. *Science* **2007**, *316* (5825), 729−732.
(12) Hiruma, K.; Yazawa, M.; Katsuyama, T.; Ogawa, K.; Haraguchi, K.; Koguchi, M.; Kakibayashi, H. *J. Appl. Phys.* **1995**, *77* (2), 447−462.
(13) Caroff, P.; Dick, K. A.; Johansson, J.; Messing, M. E.; Deppert, K.; Samuelson, L. *Nat. Nanotechnol.* **2009**, *4* (1), 50−55.
(14) Kim, D. S.; Scholz, R.; Gösele, U.; Zacharias, M. *Small* **2008**, *4* (10), 1615−1619.
(15) Colli, A.; Hofmann, S.; Ferrari, A. C.; Ducati, C.; Martelli, F.; Rubini, S.; Cabrini, S.; Franciosi, A.; Robertson, J. *Appl. Phys. Lett.* **2005**, *86* (15), 153103.
(16) Lehmann, O.; Stuke, M. *Science* **1995**, *270* (5242), 1644−1646.
(17) Wanke, M. C.; Lehmann, O.; Müller, K.; Wen, Q.; Stuke, M. *Science* **1997**, *275* (5304), 1284−1286.
(18) Cao, L.; Barsic, D. N.; Guichard, A. R.; Brongersma, M. L. *Nano Lett.* **2007**, *7* (11), 3523−3527.
(19) Boyd, D. A.; Greengard, L.; Brongersma, M.; El-Naggar, M. Y.; Goodwin, D. G. *Nano Lett.* **2006**, *6* (11), 2592−2597.
(20) Kim, B. J.; Wen, C.-Y.; Tersoff, J.; Reuter, M. C.; Stach, E. A.; Ross, F. M. *Nano Lett.* **2012**, *12* (11), 5867−5872.
(21) Gamalski, A. D.; Tersoff, J.; Sharma, R.; Ducati, C.; Hofmann, S. *Nano Lett.* **2010**, *10* (8), 2972−2976.
(22) Okamoto, H.; Massalski, T. B. *Bull. Alloy Phase Diagrams* **1984**, *5* (6), 601−610.
(23) Zhao, Q.; Zhou, J.; Zhang, F.; Lippens, D. *Mater. Today* **2009**, *12* (12), 60−69.
(24) Huang, L.; Yu, Y.; Cao, L. *Nano Lett.* **2013**, *13* (8), 3559−3565.
(25) Fu, Y. H.; Kuznetsov, A. I.; Miroshnichenko, A. E.; Yu, Y. F.; Luk'yanchuk, B. *Nat. Commun.* **2013**, *4*, 1527.
(26) Cao, L.; White, J. S.; Park, J.-S.; Schuller, J. A.; Clemens, B. M.; Brongersma, M. L. *Nat. Mater.* **2009**, *8* (8), 643−647.
(27) van de Groep, J.; Polman, A. *Opt. Express* **2013**, *21* (22), 26285−26302.
(28) Michaelis, F. B.; Weatherup, R. S.; Bayer, B. C.; Bock, M. C. D.; Sugime, H.; Caneva, S.; Robertson, J.; Baumberg, J. J.; Hofmann, S. *ACS Appl. Mater. Interfaces* **2014**, *6* (6), 4025−4032.
(29) Bock, M. C. D.; Denk, R.; Wirth, C. T.; Goldberg-Oppenheimer, P.; Hofmann, S.; Baumberg, J. J. *Appl. Phys. Lett.* **2012**, *100* (1), 013112.
(30) Ferreira, P. j.; Mitsuishi, K.; Stach, E. a. *MRS Bull.* **2008**, *33* (02), 83−90.
(31) Ziegler, C.; Eychmüller, A. *J. Phys. Chem. C* **2011**, *115* (11), 4502−4506.

DOI: 10.1021/acs.nanolett.5b02953
Nano Lett. 2015, 15, 7452−7457